



Plastic Deformation Effect on Wear and Corrosion resistance of Super Martensitic Stainless Steel

C. E. Ramoul^{1,2} · O. Ghelloudj¹ · A. Gharbi¹ · S. Tlili¹ · N. E. Beliardouh² · T. Chouchane¹

Received: 25 February 2021 / Revised: 17 May 2021 / Accepted: 8 June 2021 / Published online: 16 June 2021
© The Author(s), under exclusive licence to Springer Nature Switzerland AG 2021

Abstract

The microstructure and the mechanical properties of a super martensitic stainless steel (SMSS) were investigated in this study. Test specimens were taken from seamless tube generally used in oil and gas industries. The specimens were plastically deformed by tension from its as-received state to different levels of elongation at 2%, 10%, and 15%, respectively. The focus was to study the influence of plastic deformation on the tribological behavior against alumina balls in dry conditions and the corrosion resistance in 3.5% NaCl solution. Analysis results showed an abrasive wear as the main wear mechanism. Plastic deformation prior to sliding wear test increases wear resistance as the deformation rate increases. Based on the electrochemical experiments, all of the specimens showed an increase in their corrosion resistance i.e., the corrosion potential E_{corr} (vs. Ag/AgCl) tends to move toward more noble values with respect to the initial potential. The greatest polarization resistance was displayed by the specimen with 10% of deformation rate.

Keywords Super martensitic stainless steel · Cold deformation · Wear · Corrosion

1 Introduction

Low-carbon super martensitic stainless steel (SMSS) conform to AISI 400, series are the most useful corrosion-resistant alloy (CRA) for casing liners and tubing in the oil and gas exploration industry. SMSS was particularly utilized in the development of deep and hot oil and gas wells due to its better reliability, mechanical properties, and high corrosion resistance compared with traditional grades of martensitic stainless steel AISI 400, 410 (UNS S41000).

Overall, the corrosion of stainless steels can be categorized as one of numerous mechanisms such as general corrosion, pitting corrosion, crevice corrosion, stress corrosion cracking, sulfide stress corrosion cracking, etc. Most reviewed papers focus on conventional environments such as NaCl in order to evaluate the tendency toward localized corrosion, or H_2SO_4 so as to test the passivity behavior. Other environments were also used in reference to specific

applications such as for food industries e.g., acetic acid [1] or for biomedical applications e.g., phosphate-buffered saline solution [2]. As regards the specific case of martensitic and super martensitic stainless steels, it is of greatest importance in the oil and gas industry to take into account the resistance of the material against sulfide stress corrosion cracking (SSCC). Moreover, during drilling, the surface of a pipe was exposed to aggressive fluid environments containing chloride, carbon dioxide, and hydrogen sulfide [3]. Solutions at pH = 3, containing 5.0 wt.% NaCl and some H_2SO_3 , maintained at 25 ± 2 °C are used in order to simulate the industrial atmosphere environment [3].

New SMSS grades (13Cr) have ultra-low-carbon content, less than 0.1 weight percent (Wt.%) and much more in nickel (3.5–4.5 Wt.%) and (1.5–2.5 Wt.%) in molybdenum content [4]. They exhibited higher resistance to sulfide stress cracking (SSCC) and higher resistance to CO_2 corrosion. An increase in Cr content 17 Wt.% (Super 17Cr AISI) with martensitic/ferritic microstructure provides enhanced corrosion, high strength, and acceptable SCC performance up to 200 °C (392°F) under mild sour conditions [5].

The chemical composition is a key factor influencing the final microstructure (after heat treatments), the mechanical properties, and the electrochemical performances. The microstructure of SMSS's after thermal

✉ C. E. Ramoul
rchems@yahoo.com; c.ramoul@crti.dz

¹ Research Center in Industrial Technologies CRTI, P.O. Box 64, 16014 Cheraga, Algiers, Algeria

² Laboratoire Ingénierie Des Surfaces (LIS), Université Badji Mokhtar, BP 12, 23000 Annaba, Algeria

treatment at high temperature is generally characterized by mixture of tempered lath martensite and reverted austenite. Chromium addition is well known as the essential element against corrosion, nickel stabilizes the austenitic structure, and avoids the δ -ferrite transformation during cooling [6]. The molybdenum addition is necessary to improve the passive film stabilization and mechanical properties. It is especially added in steels intended for the transport of gas and oil [7, 8]. These alloying elements have been proved to have satisfying performances under high-temperature and high-pressure environment. Elements such as titanium and niobium can be added to further increase the mechanical properties by reacting with carbon to form carbides or carbo-nitrides resulting in an increase in strength. It was reported that 0.1% of Nb led to increasing hardness and yield strength [9]. Several studies on the SMSS have indicated that heat treatments have a significant effect on microstructures and properties. Nowadays, the improvement effects of the microstructural components of SMSS (lath martensite matrix, reversed austenite, carbides and second phase precipitations) on the comprehensive properties of the materials are well known.

In contrast, only a few studies have been conducted so far on the tribological behavior of SMSS, priority is given to corrosion resistance, shock resistance, and high plasticity. However, during oil exploitation, the operating conditions can damage the external and internal parts of pipe (SMSS) by erosion and abrasive wear [10, 11]. SMSS presented a poor wear resistance that is why the strategy calls for a superficial thermochemical treatment e.g., nitriding [12]. The high surface hardness can resist the plastic deformation and the high compressive residual stresses during wear [12, 13].

In previous work [14], characterization of wear and corrosion are conducted on specimens after heat treatments. In this work, a mechanical pre-treatment (plastic deformation) was applied to an industrial SMSS at standard annealing state. The wear performances against alumina ball and the corrosion resistance against chloride ions are analyzed and discussed. This material is used in oil well casings for drilling in the Algerian desert by the national oil company, SONATRACH. Therefore, recycling this material is of great importance. The goal was to explore the possibility to use SMSS material, released by conventional oil and gas extraction, in other applications such as industrial knives and domestic cutlery, parts of machines that work in agriculture, public works, and building. That is why, it was important to experiment the cold plastic deformation on the mechanical and chemical performances of this kind of steel. The scope of this current work is an attempt to solve a recycling problem based on adequate mechanical pre-treatment. Besides, to our knowledge, no data about the tribological contact studied here were reported in the literature so far.

2 Experimental Procedure

Samples were taken at the state provided by the manufacturer, in the longitudinal direction of a pipe, machined to obtain standard specimens, and do not undergo any heat treatment.

The chemical composition (in wt.%) was C (0.018), Si (0.0215), Mn (0.411), P (0.011), S (0.004), Cr (12.25), Ni (5.45) Mo (2.06), Cu (0.245), and Fe (Bal.). Tensile tests (*EN ISO6892-1* norm, *Zwick Z1200* testing machine) were used to apply different deformation rates to the specimen until rupture. Samples destined for tribological tests are rods having 15 mm in diameter and 6.3 mm in thickness. Before any test, samples are polished using traditional protocol to a final roughness of $R_a \sim 0.05 \mu\text{m}$. An optical microscope (*Nikon ECLIPSE LV 100ND*) was used to analyze the microstructures after electrochemical attack in 10% of oxalic acid solution for 60 s at 1.5 V.

The X-ray diffraction (XRD) analysis has been carried out at ambient temperature by means of *RIGAKU Ultima IV* diffractometer using Cu ($K\alpha$) source radiation at scan rate of 0.05°s^{-1} between angles of 20° – 90° .

The tribological tests were carried out using a ball-on-disk configuration (*CSM Instrument tribometer*) at room temperature and relative humidity of 40–50%, under 5 N of applied load, 2 cm/s of linear speed, and 20 m of total sliding distance (The Hertzian max pressure $\sim 1 \text{ GPa}$) in accordance with the ASTM G 99 standards [15]. The chosen counterpart was an alumina ball provided by *CSM Instrument* (Hardness = 13 GPa). Specific wear rate was evaluated using conventional formula as follows [16]:

$$W_s = \frac{V}{NL} (\text{mm}^3/\text{Nm}) \quad (1)$$

where W_s is the specific wear rate, V is the wear volume [mm^3], N is the normal load [N], and L is the sliding distance [m]. An optic interferometric profilometer (*WYKO, NT1100 VEECO*) was used to calculate the wear volume via a short software. An automatic (*Wylson*) micro-hardness system (300 g of load, during 10 s) was employed to measure hardness inside the worn surfaces of samples. Scanning Electron Microscopy system coupled with an Energy Dispersive X-ray spectrometer (*Jeol, JSM 7800F*) was employed at an accelerating voltage of 5 kV and secondary electron (SE) imaging type to analyze the wear mechanisms.

Corrosion tests were carried out with *Autolab* potentiostat/galvanostat and a conventional three-electrode cell with the sample as the working electrode (WE), an Ag/AgCl electrode as the reference electrode (RE), and platinum electrode as the counter electrode (CE) in 100 ml of 3.5 wt% NaCl solution. Potentiodynamic polarization was performed at room temperature (23°C) at a scan rate of 1 mV/s with

the potential range from -1 to $+1$ V. Before polarization measurements, the open circuit potentials (OCPs) of all the worked electrodes were monitored for 1 h to attain stable OCP. It has been found that the OCP stabilizes around -320 mV after 30 min indicating that a passive film strives to be formed.

3 Results and Discussion

3.1 Microstructure and Mechanical Properties

Figure 1 demonstrates an example of stress–strain curve of SMSS obtained in this study. The labels (A, B, C, and D) indicated the position of sampling procedure. The initial state sample (without plastic deformation) is noted “A”, while samples B, C, and D correspond to 2%, 10%, and 15% of deformation rates, respectively. Results of the tensile test at rupture are 706 ± 3 MPa of yield strength, 791 ± 6 MPa of tensile strength, and 15 ± 1 of elongation. This results are in good agreement with those reported in the literature [17, 18]. Vickers hardness values ($HV_{0.3}$) are 280, 289, 310, and 303, respectively, for A, B, C, and D specimens, respectively.

Figure 2 shows the XRD spectra of the as-received SMSS's sample. It reveals only peaks of the α -Fe solid solution (ferrite). The quantitative analysis revealed the nature and proportions of the existing microstructural phase. The steel is composed of 99.91% α -Fe and the rest (0.09%) is carbides (most probably cementite (Fe, Cr)₃C type).

Figure 3 shows optical microstructure analysis of the samples, at initial state (Fig. 3a), and after different deformation rates (Fig. 3b–d) in accordance to the positions A, B, C, and D (Fig. 1). Initial microstructure is mainly composed of equiaxial grains of ferrite (α -Fe) and intergranular precipitation of a secondary phase may be cementite (Fe, Cr)₃C and $M_{23}C_6$ type [19]. Furthermore, Fig. 3 reveals a slight difference from the basic microstructure (Fig. 3b–d).

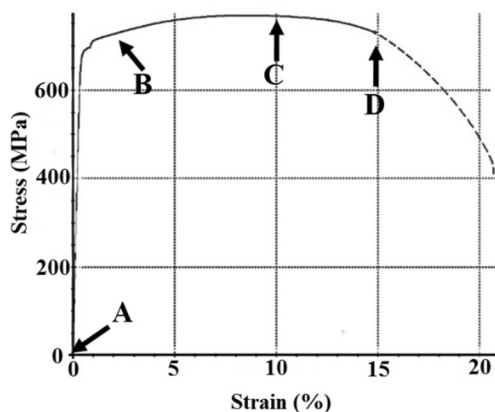


Fig. 1 Stress–strain curve of super martensitic stainless steel

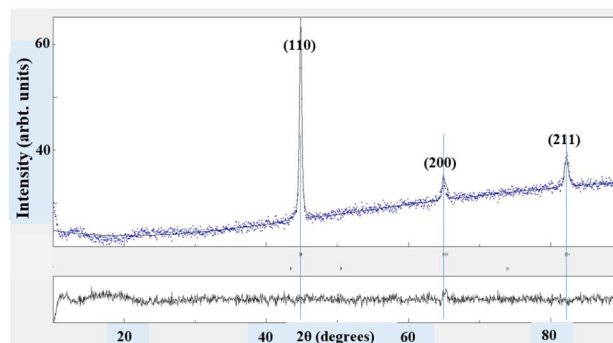


Fig. 2 X-ray spectrum of SMSS steel of the as-received sample

Cold plastic deformation provokes the strain-hardening of the microstructure i.e., an increase in grain boundaries density (reduction in grain sizes) and an increase in density of dislocations and other microstructural defects. Besides, the quantity of pits and holes (black dots showed by yellow narrows on optical micrographs) increases as a consequence of localized corrosion attack during electrochemical etching by oxalic acid.

3.2 Tribological Behavior

3.2.1 Coefficient of Friction (COF) Evolution

Figure 4 shows the coefficient of friction evolution of different samples against alumina ball in dry conditions. One can see that all of the tested samples display similar curve tendencies characterized by two steps. The first one is a short run-in (< 1 m of sliding distance). The run-in period (first stage) corresponds to the contact between hard asperities of alumina ball rubbing against steel surface. Figure 4 also shows a “transitional period” between the first and the second step. In this period, the COF of all tested samples shows a decreasing trend or rapid drop between 2.5 m and 4 m. This phenomenon may be related to an oxide film formation. After several sliding cycles, this film becomes brittle and transforms into wear debris, which acted as a solid lubricant leading to the decrease in COF during a short period. After that, the COF abruptly increases to higher values (> 5 m). It represents the beginning of the second step or the steady state. This is the consequence of the increase in friction force; the wear mechanism becomes an aggressive wear and after that the COF stabilizes finally around (0.7–0.8) values. Much higher value (0.9) was observed in the sample B (2% case).

Optic microscopy analysis reveals different aspects of worn surfaces as can be seen in Fig. 5a–d (=OM of wear scars after sliding test). A comparative study needs a quantitative estimation of the wear volume. Figure 5a', b', c', and d' presented the optic images (3D profile) of the wear

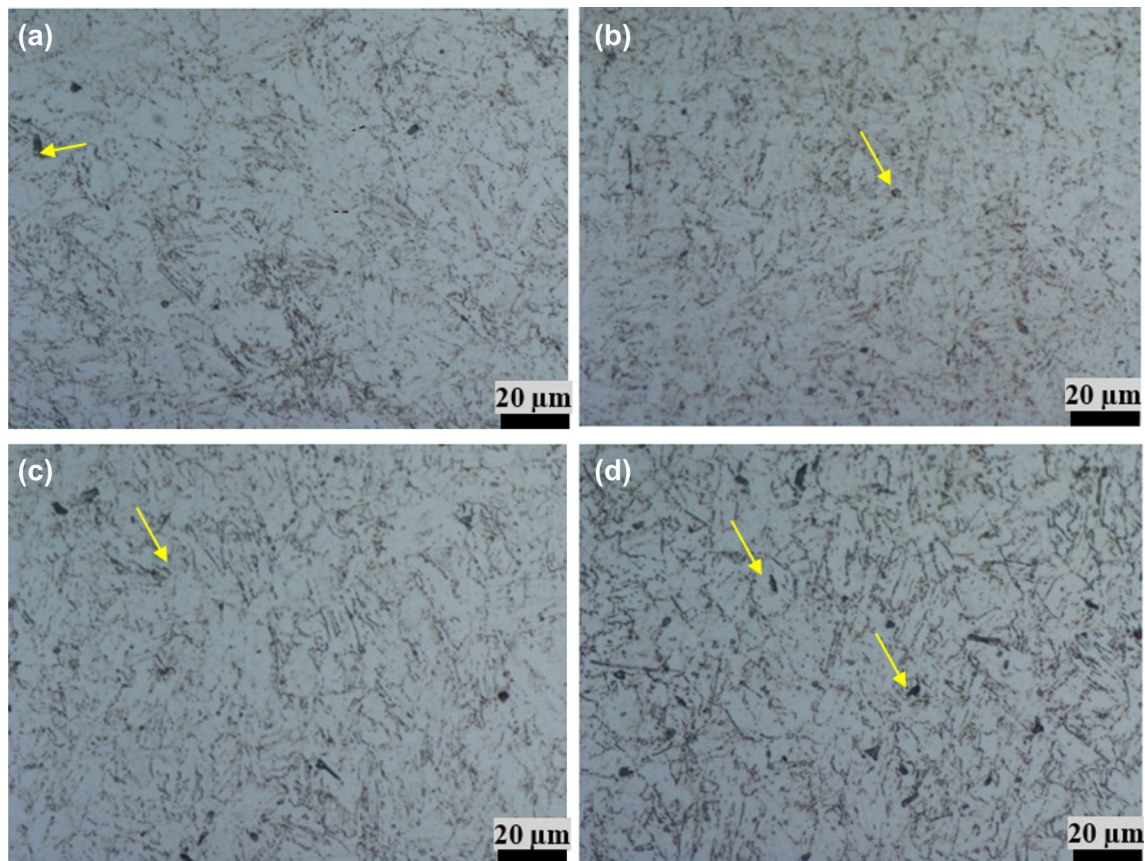


Fig. 3 Optical micrographs of super martensitic stainless steel at initial state (a), after 2% (b), 10% (c), and 15% (d) of strain deformation at ambient temperature

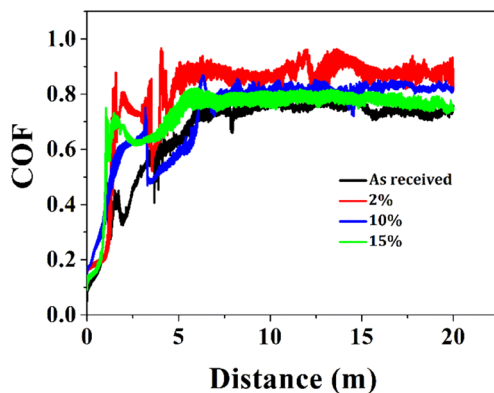


Fig. 4 Coefficient of friction evolution of the tested specimens

scars obtained by means of an optical profilometer. It can be seen that the highest dimensions (depth and width) i.e., wear volume were found for samples deformed at 2% (sample B). The quantitative results of the specific wear rate are presented in Table 1. One can note that harness has increased even further inside the wear track. The increase in harness

leads to a decrease in wear volume as expected. As mentioned above, the wear volume of sample B is one-and-a-half time higher than that of sample D.

3.2.2 Worn Surface Analysis

Figure 6 shows SEM micrographs and EDX analysis of the worn surface of tested specimens. The wear track analysis indicated that specimen's surfaces have undergone severe wear after 20 m of sliding distance. SEM micrographs revealed grooves, debris, and holes. Surface aspects presented in Fig. 6 are consequences of different phenomena that occur during rubbing against alumina ball.

In overall, the samples have displayed similar behavior i.e., a severe abrasive wear characterized by intensive oxidation, plastic deformation, and abrasion. During sliding, rubbing of the counter body increases the temperature of the two surfaces in contact, thus provoking tribo-chemical reactions (oxidation). After more and more cycles, oxide film formation occurs at the top surface layer and immediately turns in debris because of its brittleness. The linear EDS scan in Fig. 6b indicates a rise in oxygen content (line

Fig. 5 Optical microscopy images (a–d) of wear scars after sliding test and the corresponding 3D profiles (a', b', c', and d') as shown, respectively, by A, B, C, and D specimens

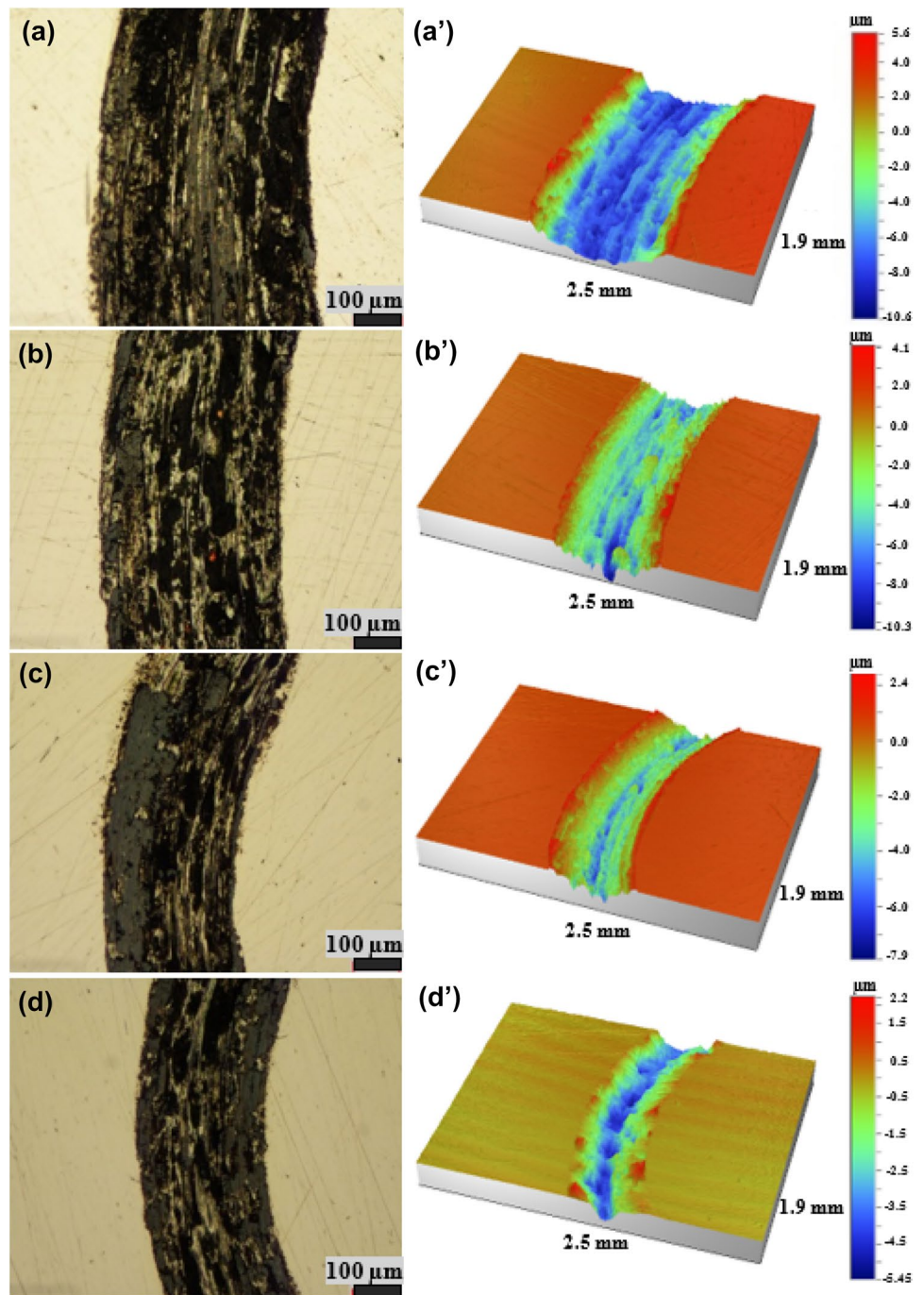


Table 1 Results of hardness measurements on disk specimens after wear test in correlation with the friction coefficient and wear rate

| Samples | Worn surface hardness (Hv) | COF | Specific wear rate 10^{-4} (mm ³ /N.m) |
|---------|----------------------------|------|---|
| (A) | 350 | 0.73 | 2.69 |
| (B) | 405 | 0.86 | 2.12 |
| (C) | 538 | 0.8 | 2.05 |
| (D) | 550 | 0.76 | 1.4 |

in blue) inside the wear scar when compared to the metal of the non-affected zone of the wear track. The final step was a third body abrasive wear.

As expected from the COF evolution (Fig. 4), the wear mechanism at the start of sliding test is a mild abrasive wear (low friction) due to the hard asperities of alumina ball rubbing against sample's surface. Next, it becomes oxidative and abrasive wear (high friction) as well described by parallel grooves in the sliding direction, due to the wear debris formation essentially composed of oxides. Finally, the

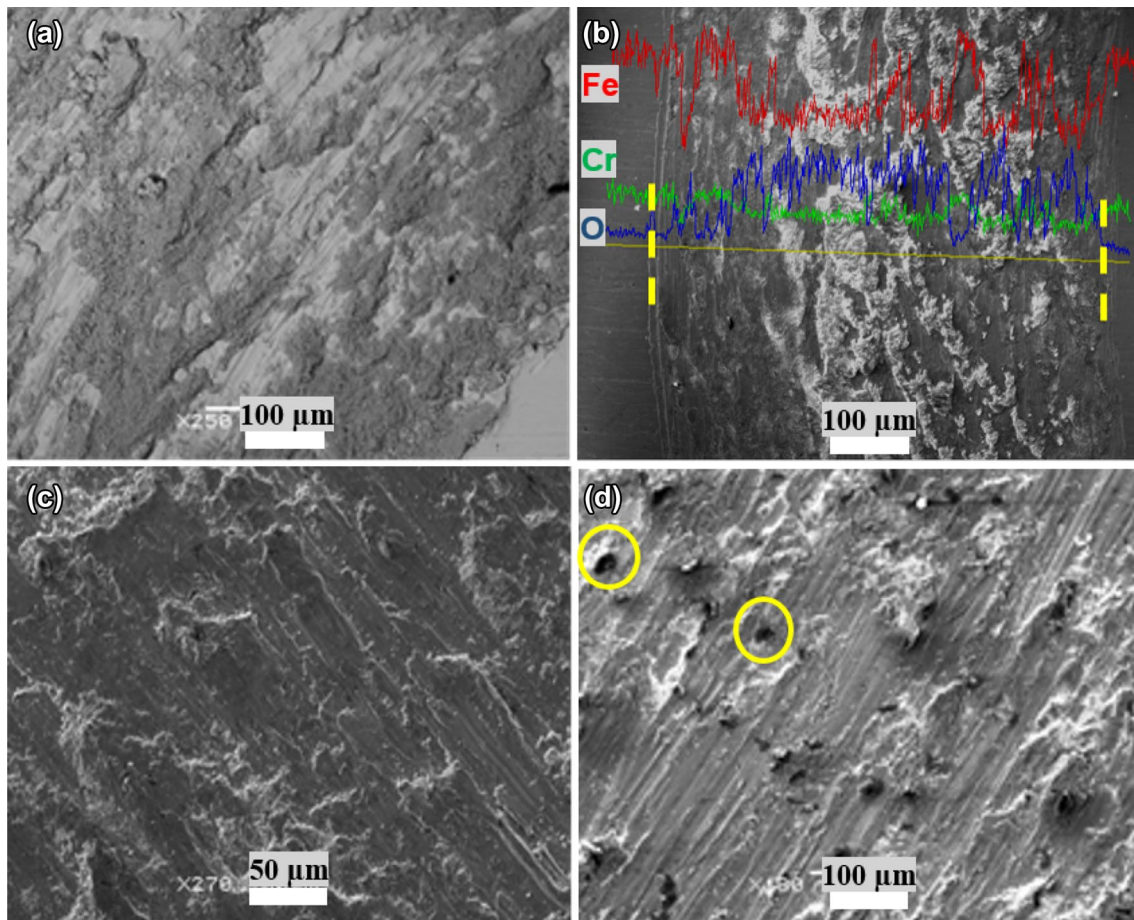
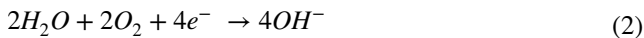


Fig. 6 a–d SEM micrographs of the worn surfaces as displayed by the tested specimens A, B, C, and D, respectively, after tribological tests

abrasive phenomenon appears to be the most dominant wear as clearly shown in Fig. 6c, d.

3.3 Corrosion Behavior

Fig. 7 shows polarization curves (Tafel plots) of SMSS in 3.5% NaCl solution. The cathodic region describes the cathodic reaction associated with reduction of dissolved oxygen to hydroxyl ions according to the following equation:



The anodic region represents the dissolution of the sample at the applied potential. The corrosion current density (I_{corr}) and the corrosion potential (E_{corr}) were calculated based on the Tafel extrapolation method. It consists on the extrapolation of the linear parts of anodic and cathodic curves at the point of convergence. A large passive cathodic region was observed for all of the samples.

These results indicate that the sample C exhibits the better electrochemical performance due to more noble corrosion potential when compared to the other samples.

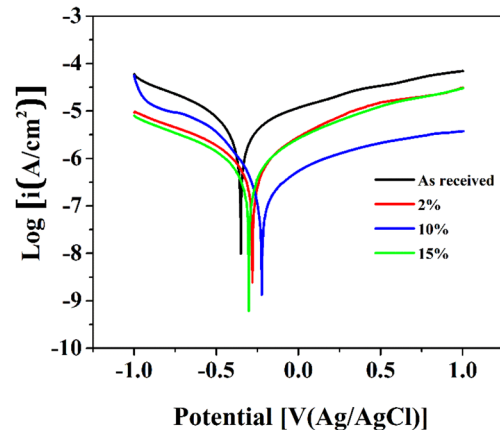


Fig. 7 Potentiodynamic polarization curve of the as-received and deformed specimens in 3.5% NaCl solution

Table 2 presents the quantitative results. It is clearly indicated that the sample A has the lowest resistance against corrosion (highest I_{corr}), while the best corrosion resistance was shown for the sample C (lowest I_{corr}). The improved

Table 2 Results deduced from potentiodynamic polarization curves of the tested specimens in 3.5% NaCl solution

| Samples | Electrochemical parameters | | | |
|---------|----------------------------|---|--------------------------|----------------------------|
| | E_{corr} (V) | I_{corr} ($\mu\text{A}/\text{cm}^2$) | Corrosion rate (mm/year) | R_p ($\text{K}\Omega$) |
| A | -0.35 | 4.83 | 0.056 | 23.78 |
| B | -0.26 | 0.45 | 0.005 | 119.33 |
| C | -0.22 | 0.17 | 0.002 | 208.76 |
| D | -0.3 | 0.24 | 0.002 | 144.85 |

polarization resistance (R_p) of SMSS is due to the formation of thick passive film rich in Cr-oxide (Cr_2O_3). It suggested a high stability of the protective film formation as reported by previous works [20]. Values of E_{corr} reported in this study are in the same range (0.2–0.35 V vs. *SCE*) of those reported by other researchers [21, 22].

4 Discussion

This study indicates an improvement in the corrosion resistance of SMSS samples after cold plastic deformation. It can look to be contradictory or unexpected result because for many materials, cold plastic deformation deteriorates the corrosion resistance such as for carbon steels. The influence of the cold work (CW) prior corrosion tests of duplex and austenitic steels was deeply investigated because of the deformation-induced martensite phenomenon. Despite this, controversies still exist.

Unfortunately, no data have been reported about CW effects on the corrosion characteristics of martensitic steels at yet. An understanding of the mechanisms involved would require a smaller-scale analysis owing to the fact that two main factors have a direct influence on the corrosion resistance of microstructure after cold plastic deformation, namely, grain size and density of dislocations. Ben Hamu et al. reported that small grain size creates more grain boundaries that act as a corrosion barrier. Inversely, high dislocation density leads to high anodic dissolution [23]. Investigating austenitic steel, Tiarniyu et al. reported that the deformed specimens were found to be more resistant to chloride-induced intergranular corrosion at room temperature compared to the undeformed ones [24]. The reason was that, the corrosion resistance of stainless steel is closely related to passive film stability. Many authors investigated the effect of grain size on corrosion of several austenitic stainless steels, claiming that the rate of uniform corrosion increases by grain size reduction, whereas the rate of intergranular corrosion is opposite [25].

It can be concluded that under the conditions studied here, corrosion characteristics analyzed by potentiodynamic

method, cold plastic deformation microstructure by tensile test lead to better corrosion resistance than undeformed one. The deformation rate seems to be an important factor that governs the film stability.

5 Conclusion

Based on the experimental results, the following conclusions can be drawn:

- The initial microstructure was dominantly constituted by ferrite ($\alpha\text{-Fe}$).
- Oxidation followed by abrasion are the main phenomena that controlled the wear mechanism in all cases, as revealed by SEM/EDS analysis. Plastic deformation prior to wear test leads to better dry sliding wear resistance.
- The sample that has undergone 10% of plastic deformation before corrosion test exhibits the highest corrosion resistance.

Acknowledgements The authors are grateful to the Directorate-General for Scientific Research and Technological Development (DGRSDT) at the Algerian Ministry of Higher Education and Scientific Research (MESRS) for its support.

Declarations

Conflict of interest On behalf of all authors, the corresponding author states that there is no conflict of interest.

References

1. Ceschini L, Chiavari C, Lanzoni E, Martini C (2012) Low-temperature carburised AISI 316L austenitic stainless steel: wear and corrosion behaviour. *Mater Des* 38:154–160. <https://doi.org/10.1016/j.matdes.2012.02.019>
2. Liu Y, Zhu D, Pierre D, Gilbert JL (2019) Fretting initiated crevice corrosion of 316LVM stainless steel in physiological phosphate buffered saline: potential and cycles to initiation. *Acta Biomater* 97:565–577. <https://doi.org/10.1016/j.actbio.2019.07.051>
3. Turnbull A, Griffiths A (2003) Corrosion and cracking of weldable 13 wt-%Cr martensitic stainless steels for application in the oil and gas industry. *Corros Eng Sci Technol* 38(1):21–50. <https://doi.org/10.1179/147842203225001432>
4. Ye D, Li J, Jiang W, Su J, Zhao K (2012) Effect of Cu addition on microstructure and mechanical properties of 15%Cr super martensitic stainless steel. *Mater Des* 41:16–22. <https://doi.org/10.1016/j.matdes.2012.04.036>
5. Hill R, Perez AL (2017) New steels and corrosion-resistant alloys. In: El-Sherik AM (ed) *Trends in oil and gas corrosion research and technologies: production and transmission*, 1st edn. Woodhead Publishing, pp 613–626
6. Mabruhi E, Anwar MS, Prifiharni S, Romijarso TB, Adjiantoro B (2016) Tensile properties of the modified 13Cr martensitic

- stainless steels. *AIP Conf Proc* 1725(1):020039-1-020039–5. <https://doi.org/10.1063/1.4945493>
7. Rodrigues CAD, Lorenzo PLD, Sokolowski A, Barbosa CA, Rollo JM (2007) Titanium and molybdenum content in supermartensitic stainless steel. *Mater Sci Eng A* 461:149–152. <https://doi.org/10.1016/j.msea.2007.01.016>
 8. Liu YR, Ye D, Yong QL, Su J, Zhao KY, Jiang W (2011) Effect of heat treatment on microstructure and property of Cr13 super martensitic stainless steel. *J Iron Steel Res Int* 18(11):60–66. [https://doi.org/10.1016/S1006-706X\(11\)60118-0](https://doi.org/10.1016/S1006-706X(11)60118-0)
 9. Ma X, Zhou C, Wang L, Liu C, Subramanian S, de Oliveira MP (2013) Role of Nb in 13Cr super-martensitic stainless steel. *Rem Rev Esc Minas* 66(2):179–185. <https://doi.org/10.1590/s0370-44672013000200007>
 10. Zepon G, Kiminami CS, Filho WJB, Bolfarini C (2013) Microstructure and wear resistance of spray-formed supermartensitic stainless steel. *Mater Res* 16(3):642–646. <https://doi.org/10.1590/S1516-14392013005000026>
 11. Barbosa C, Abud I (2013) Recent developments on martensitic stainless steels for oil and gas production. *Recent Patents Corros Sci* 3(1):27–38. <https://doi.org/10.2174/22106839112029990004>
 12. Sun Y, Bell T, Wood G (1994) Wear behaviour of plasma-nitrided martensitic stainless steel. *Wear* 178(1–2):131–138. [https://doi.org/10.1016/0043-1648\(94\)90138-4](https://doi.org/10.1016/0043-1648(94)90138-4)
 13. Xi YT, Liu DX, Han D (2008) Improvement of corrosion and wear resistances of AISI 420 martensitic stainless steel using plasma nitriding at low temperature. *Surf Coatings Technol* 202(12):2577–2583. <https://doi.org/10.1016/j.surfcoat.2007.09.036>
 14. Beliardouh NE, Tlili S, Oulabbas A, Ramoul CE, Meddah S, Kaleli H (2021) Investigation on dry sliding wear performance and corrosion resistance of 13Cr5Ni2Mo supermartensitic stainless steel. *Tribol Ind* 43(1):107–116. <https://doi.org/10.24874/ti.970.09.20.11>
 15. Ramoul C, Beliardouh NE, Bahi R, Nouveau C, Djahoudi A, Walock MJ (2019) Surface performances of PVD ZrN coatings in biological environments. *Tribol Mater Surfaces Interfaces* 13(1):12–19. <https://doi.org/10.1080/17515831.2018.1553820>
 16. Tlili S, Beliardouh NE, Ramoul CE, Bahi R, Abdullah OI, Kaleli H, Samad MA (2018) Thermal treatment effect on tribological and corrosion performances of 13Cr5Ni2Mo super-martensitic stainless steel. *Tribol Ind* 40(3):433–439. <https://doi.org/10.24874/ti.2018.40.03.09>
 17. Oliveira MP, Calderón-Hernández JW, Magnabosco R, Hincapie-Ladino D, Alonso-Falleiros N (2017) Effect of niobium on phase transformations, mechanical properties and corrosion of supermartensitic stainless steel. *J Mater Eng Perform* 26(4):1664–1672. <https://doi.org/10.1007/s11665-017-2610-1>
 18. Niessen F (2018) Austenite reversion in low-carbon martensitic stainless steels—a CALPHAD-assisted review. *Mater Sci Technol* 34(12):1401–1414. <https://doi.org/10.1080/02670836.2018.1449179>
 19. Lacombe P, Baroux B, Béranger G (1990) *Les aciers inoxydables*. Les Ulis, Paris
 20. Rodrigues CAD, Bandeira RM, Duarte BB, Tremiliosi-Filho G, Jorge AM (2016) Effect of phosphorus content on the mechanical, microstructure and corrosion properties of supermartensitic stainless steel. *Mater Sci Eng A* 650:75–83. <https://doi.org/10.1016/j.msea.2015.10.013>
 21. Ma XP, Wang LJ, Liu CM, Subramanian SV (2012) Microstructure and properties of 13Cr5Ni1Mo0.025Nb0.09V0.06N super martensitic stainless steel. *Mater Sci Eng A* 539:271–279. <https://doi.org/10.1016/j.msea.2012.01.093>
 22. Kang J, Li J, Zhao KY, Bai X, Yong QL, Su J (2015) Passivation behaviors of super martensitic stainless steel in weak acidic and weak alkaline NaCl solutions. *J Iron Steel Res Int* 22(12):1156–1163. [https://doi.org/10.1016/S1006-706X\(15\)30127-8](https://doi.org/10.1016/S1006-706X(15)30127-8)
 23. Hamu GB, Eliezer D, Wagner L (2009) The relation between severe plastic deformation microstructure and corrosion behavior of AZ31 magnesium alloy. *J Alloys Compd* 468(1–2):222–229. <https://doi.org/10.1016/j.jallcom.2008.01.084>
 24. Tihamiyu AA, Eduok U, Odeshi AG, Szpunar JA (2019) Effect of prior plastic deformation and deformation rate on the corrosion resistance of AISI 321 austenitic stainless steel. *Mater Sci Eng A* 745:1–9. <https://doi.org/10.1016/j.msea.2018.12.093>
 25. Miyamoto H (2016) Corrosion of ultrafine grained materials by severe plastic deformation, an overview. *Mater Trans* 57(5):559–572. <https://doi.org/10.2320/matertrans.M2015452>

Publisher's Note Springer Nature remains neutral with regard to jurisdictional claims in published maps and institutional affiliations.